# First-Principles Modeling of a Dye-Sensitized TiO₂/IrO₂ Photoanode for Water Oxidation

Mariachiara Pastore* and Filippo De Angelis*

Computational Laboratory for Hybrid Organic Photovoltaics (CLHYO), CNR-ISTM, via Elce di Sotto 8, I-06123 Perugia, Italy

Ⓢ Supporting Information

ABSTRACT: We present a first-principle computational modeling investigation, based on density functional theory (DFT) and time-dependent DFT, on the structural, electronic, optical, and charge generation properties of the semiconductor/dye/catalyst heterointerfaces in a prototypical dye-sensitized photoanode for water oxidation. The investigated architecture comprises a Ru(II) dye-sensitized TiO₂ substrate tethered to an IrO₂ nanoparticle catalyst. Our realistic modeling strategy and quantitative analysis of the relevant interfacial hole/electron transfer reactions indicates the slow hole injection into IrO₂ and the fast dye excited-state quenching to IrO₂ as the primary sources of the relatively poor cell efficiency experimentally observed. On the basis of this atomistic and electronic structure information, we propose and computationally test, against a prototype dye, a new class of Ru(II) sensitizers, which show potentially improved photoelectrochemical performances. This study constitutes a first step toward the computer-assisted design of new and more efficient materials for solar fuels production through dye-sensitized photoelectrochemical cells.
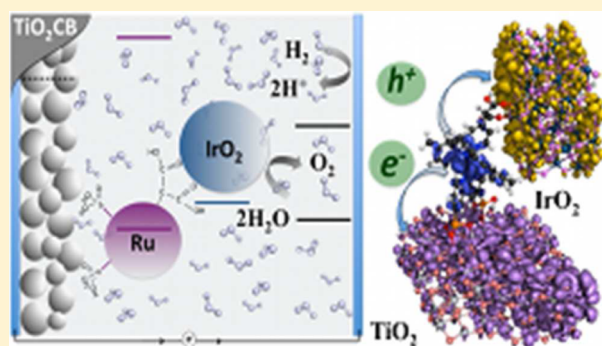
1. INTRODUCTION

One of the greatest scientific and technological challenges facing humanity is to capture and convert solar energy into electricity[1] or to store it into chemical fuels, producing hydrogen (or other reduced fuels) and oxygen from water.[2−4] Solar hydrogen generation from water is a very attractive field of research, allowing the production of inexhaustible renewable fuel without emission of pollutants and greenhouse gases. The reactions taking place at the electrodes of a photoelectrochemical cell (PEC) are reported in the following, where h⁺ and e⁻ are, respectively, the photogenerated holes and electrons:

$$2H_2O + h\nu + 4h^+ \rightarrow O_2 + 4H^+ \quad E^0 = 1.23 \text{ V vs NHE}$$

$$4H^+ + 4e^- \rightarrow 2H_2 \quad E^0 = 0 \text{ V vs NHE}$$
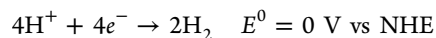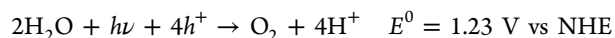
The first example of a water splitting PEC was reported in 1972 by Fujishima and Honda:[5] A semiconducting TiO₂ photoanode was irradiated with UV light, producing oxygen at the anode and hydrogen at a platinum cathode. Since this observation, over the last 40 years, the development of photocatalytic semiconducting metal oxides has represented a very active research field, with many reported systems showing high photocatalytic activities.[6−8] The main limitation of these oxides is that they are only active under UV irradiation, thus exploiting only a minor fraction (ca. 4%) of solar power. The development of stable and highly efficient visible-light-driven photocatalysts has, therefore, represented a crucial issue in the attempt of enhancing semiconductor-based photo-catalytic water splitting.[9−14]

A different approach to visible-light water splitting relies on the use dye-sensitized semiconductor nanoparticles, linked to an oxygen evolving catalyst.[15−24] In this type of PEC, directly related to the dye-sensitized solar cell, a dye adsorbed on the surface of a wide band gap semiconductor (typically TiO₂) absorbs the solar radiation to produce an electron and a hole, which are injected into the semiconductor and catalyst, respectively. In such a dye-sensitized PEC (DSPEC) oxygen is produced at the dye-sensitized semiconductor photoanode, while hydrogen is produced by a catalyst at the cathode, where photogenerated electrons are collected.

While the development of catalysts and sensitizers for the proton reduction half reaction has achieved a significant progress over the last years,[25] the four-electron water oxidation reaction represents the main barrier toward the design of efficient and stable water splitting devices. Individual characteristics of water oxidation catalysts (WOCs), photosensitizers, and semiconductors as well as the interfacial properties of the assembled photoanodes strongly interplay in determining the quantum (percentage conversion of photons to hole−electron pairs) and Coulombic (percentage conversion of 4 hole−electrons pairs into O₂ molecules) efficiencies.[2] Both molecular[26−37] and heterogeneous metal-oxide[38−42] WOCs have been reported so far. Molecular (homogeneous) WOCs, while offering the advantages of a larger structural variability and of an easier kinetic and mechanistic characterization, are often unstable and labo-

Scheme 1. (a) Scheme of a Prototypical DSPEC[16] along with Main Energy Levels and Relevant Electron Transfer Processes[a] and (b) Molecular Structure of Dye1
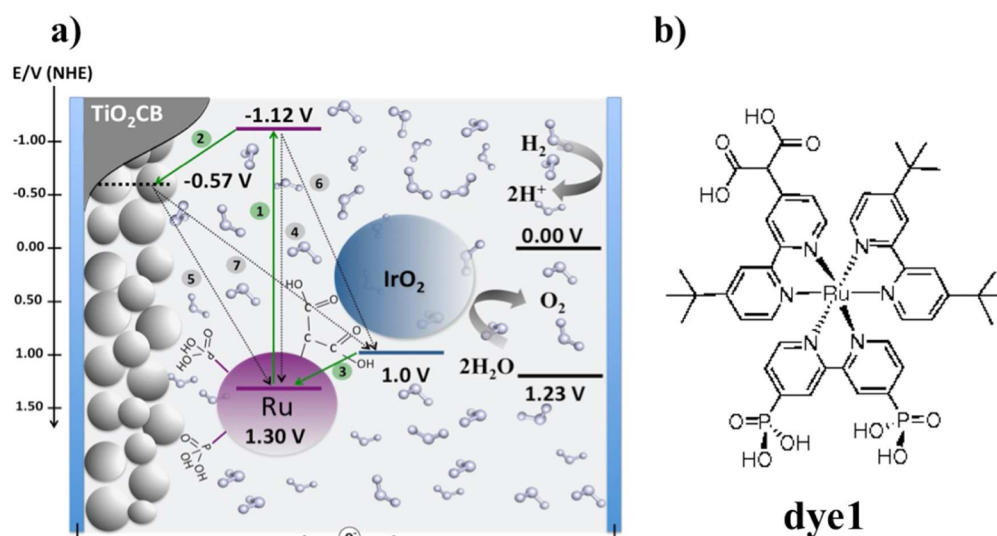
[a](1) Dye photoexcitation; (2) electron injection/semiconductor reduction; (3) hole injection/catalyst oxidation; (4) dye radiative or nonradiative recombination; (5) electron−hole recombination to the oxidized dye; (6) oxidative dye excited-state quenching to the catalyst; (7) electron−hole recombination to the oxidized catalyst.

rious to synthesize. On the other hand, metal-oxide nanoparticle WOCs, such as RuO_2 and IrO_2, are synthetically easy to obtain and generally stable, although their structural and operational characterization is not straightforward. Iridium oxide, both in its crystalline (IrO_2) and amorphous colloidal ($IrO_2 \cdot nH_2O$) form, is a central player in the development of photoanodes for water oxidation.[15,16,21,43−48] This unsurpassed success, only recently matched by optimized perovskite transition metal oxides,[49] is mainly due to its relatively low overpotential for water oxidation (0.2−0.3 V) over a large pH range with a high turnover frequency (TOF) of 40 s^{-1}.[17] The sensitizing dye characteristics are also central to the DSPEC efficiency. Optimal dyes should possess: (i) wide and intense absorption in the visible and possibly near-infrared region; (ii) sufficiently long-lived charge separated excited state to inject the photoexcited electrons into the conduction band (CB) semiconductor; and (iii) appropriate redox potential to sustain the catalytic water oxidation along with stable anchoring to the semiconductor surface in the oxidative PEC environment.

To date, the most widely employed DSPEC sensitizers are $[Ru(bpy)_3]^{2+}$ derivatives[50] or porphyrin-based compounds,[51−53] properly modified to be effectively grafted on water splitting photoanodes. On the semiconductor side, due to the instability of ZnO in acidic conditions, mesoporous TiO_2 or hybrid core−shell ZnO-TiO_2 and $CdSe/TiO_2$ nanostructures are the materials of choice.[17,42,54,55] Despite substantial research efforts, the effective integration of sensitizers, WOCs and semiconductors into efficient photoanodes for water oxidation is still a challenge, and only few complete systems have been reported so far.[15,18,19,20,21,34,56,57,58] The first assembled molecular photoanode was reported in 2009 by Mollouk and co-workers,[15] employing a bifunctional heteroleptic Ru(II) sensitizer, showing phosphonate groups for TiO_2 anchoring, and a malonate group to bind to hydrated iridium oxide ($IrO_2 \cdot nH_2O$) nanoparticles (dye1 in Scheme 1).

As schematically depicted by the green arrows in Scheme 1, the forward intramolecular and interfacial hole/electron transfer

processes occurring at the photoanode (besides the four electron water oxidation process) are:

1) $Dye + h\nu \rightarrow Dye^*$ (*dye photoexcitation*)

2) $Dye^* + TiO_2 \rightarrow Dye (h^+) + TiO_2 (e^-)$ (*electron injection/semiconductor reduction*)

3) $Dye (h^+) + IrO_2 \rightarrow Dye + IrO_2 (h^+)$ (*hole injection/catalyst oxidation*).

The parasitic processes contributing to decrease the DSPEC efficiency, represented by dotted gray arrows in Scheme 1, are instead:

4) $Dye^* \rightarrow Dye + energy$ (*dye radiative or non radiative recombination*)

5) $TiO_2 (e^-) + Dye (h^+) \rightarrow TiO_2 + Dye$ (*electron-hole recombination to the oxidized dye*)

6) $Dye^* + IrO_2 \rightarrow Dye (h^+) + IrO_2 (e^-)$ (*oxidative dye excited state quenching to the catalyst*)

7) $TiO_2 (e^-) + IrO_2 (h^+) \rightarrow TiO_2 + IrO_2$ (*electron-hole recombination to the oxidized catalyst*)

Under light irradiation, this type of DSPEC produced both oxygen and hydrogen, even if low internal quantum yield and Coulombic efficiency (about 0.9% and 20%, respectively) were reported.[15] The non optimal device performances were mainly attributed to a slow hole transfer from the oxidized dye to the catalyst (process 3), which in turn favored a high back recombination from TiO_2 to the oxidized dye (process 5). A fast dye's excited-state quenching by $IrO_2 \cdot nH_2O$ has also been envisioned[59] as a possibly additional deactivation channel. Incorporation of a biomimetic electron mediator between the catalyst and the dye was found to enhance the hole transfer rate between Ru(III) and Ir(IV), determining a 3-fold increase in the photoanode efficiency.[21] Recently, with the aim of increasing the photocatalytic activity per surface iridium atom, the carboxylic-phosphonic capping of the ($IrO_2 \cdot nH_2O$) nanoparticles was eliminated by directly sintering the catalyst onto the TiO_2 surface;[46,48] the proposed architecture, however, suffered of fast $TiO_2 (e^-)$ to $IrO_2 (h+)$ recombination, cf. process 7).

This analysis draws out the key problems in this kind of device: (i) the structural, electronic, and charge transfer properties of the semiconductor/dye/WOC interfaces; (ii) stable adsorption and coadsorption, with an optimal ratio, of dye and catalyst or dye−catalyst assemblies[60] on the oxide surface; and (iii) the energy

level matching and electronic coupling, influencing the kinetics of the forward and backward electron transfers.

Computational modeling has had a great impact in dye-sensitized solar cells technology. Simulation of isolated device components as well as of the relevant interfaces ruling the devices operational mechanisms has successfully supported experimental research by providing molecular design rules of new materials and a deeper understanding of the chemical and physical processes governing the complex cell interfaces.[61,62] A comparable understanding of DSPEC is still lacking, especially for what concerns the interfacial (e^-/h^+) transfer phenomena, which are central to the efficient device functioning. Most of previous computational modeling studies, indeed, focused on the characterization of the water oxidation reaction mechanism,[63−67] with only a few investigations devoted to the interaction between the WOC and the semiconductor.[26,68]

With the aim of providing the fundamental understanding underlying the rate of the forward (e^-/h^+) transfer processes and effectively suppressing the undesired parasitic recombination reactions, here we report a fully first-principles modeling of a DSPEC photoanode comprising a ruthenium dye-sensitized TiO$_2$ model tethered to an IrO$_2$ nanoparticle catalyst. To our knowledge, this is the first computational study to address the nature of IrO$_2$ nanoparticles and to model their use as catalysts in a DSPEC. Based on such realistic model, we investigate all the relevant interfacial (e^-/h^+) transfers by hybrid DFT calculations in solution, determining the interplay of structural and electronic factors affecting the DSPEC efficiency. With this information at hand, we design a novel class of Ru(II) sensitizers rooted onto sound and documented synthetic chemical strategies, and we computationally investigate their performance in a DSPEC architecture against the parent dye1, see Scheme 1. Rewardingly, our results for the new dye show potentially improved photo-electrochemical performances, casting the desired design rules for new and more efficient devices.

2. COMPUTATIONAL DETAILS

Based on our previous expertise, TiO$_2$ was modeled by a neutral stoichiometric (TiO$_2$)$_{82}$ cluster of ca. 2 × 2 nm side, obtained by appropriately "cutting" an anatase slab exposing the majority (101) surface.[69,70] This cluster model allows us to employ hybrid functionals and continuum solvation models, providing energy levels in close agreement with experimental band edges of anatase TiO$_2$.[71,72] To our knowledge, IrO$_2$ nanoparticles have never been simulated. After testing various models, all extracted from a rutile (110) surface slab cut from the bulk, we opted for a Ir$_{56}$O$_{114}$H$_4$ neutral cluster, formally (IrO$_2$)$_{56}$·2H$_2$O, which represented a good compromise between system dimensions (ca. 1 × 1 × 0.5 nm) and accuracy in the structural (majority (110) rutile surfaces), electronic (band edges), and optical (UV−vis) properties of experimentally characterized IrO$_2$ systems, see below.

Ground-state equilibrium geometry of stand-alone dyes, IrO$_2$ and TiO$_2$ models as well as dye-TiO$_2$, dye-IrO$_2$ and TiO$_2$/dye/IrO$_2$ assemblies were optimized in the gas phase with the ADF program package,[73] using the Becke−Perdew exchange−correlation functional[74,75] and a double-ζ basis set. DFT electronic structure and TDDFT excited-state calculations in water solution were carried out on the optimized systems using the hybrid B3LYP functional together with a polarizable continuum model of solvation (C-PCM)[76,77] as implemented in the Gaussian09 suite of programs.[78] Single point calculations on the TiO$_2$/dye/IrO$_2$ and on the smaller dye-TiO$_2$ and dye-IrO$_2$ assemblies were performed employing a 6-311G** basis set for the dye atoms, with the LanL2 pseudopotential for Ru, a LanL2DZ basis set, and pseudopotentials[79−82] for the IrO$_2$ nanoparticle and a 3-21G* basis set for TiO$_2$, which was previously shown to deliver accurate excited-state energy levels for dye-sensitized TiO$_2$.[71,72] TDDFT excited-state calculations for the dye-TiO$_2$ and dye-IrO$_2$ assemblies were

performed with a 3-21G* and with LanL2DZ basis and pseudopotential, respectively, thus using a smaller basis set for the dye only compared to the larger assemblies for computational convenience.

To evaluate the electronic coupling between the dye's, semiconductor, and catalyst electronic states and thus to estimate the associated injection rates, we resorted to a Fermi golden rule framework, where the (e^-/h^+) injection rate k_{inj} is defined as

$$k_{inj} = \frac{2\pi}{\hbar} \sum_k |V_{dk}|^2 \rho(\varepsilon_k) \tag{1}$$

where the k sum runs over the manifold of TiO$_2$ or IrO$_2$ acceptor states of interest and d is the dye donor state. The $|V_{dk}|^2 \rho(\varepsilon_k)$ product is the probability distribution $\Gamma(\varepsilon_k)$. The inverse of k_{inj} is the injection time τ. To evaluate the diabatic states needed to calculate the coupling matrix elements V_{dk} and partial density of states (DOS) $\rho(\varepsilon_k)$, we adopted the model proposed by Thoss et al.[83,84] and recently applied to the dye/TiO$_2$ interfaces in dye-sensitized solar cells.[85,86] This approach is based on the localization of the molecular orbitals of the entire complex on the donor and acceptor species, resulting in a block Fock matrix of the interacting system, where the diagonal elements represent the energies of the localized states, while the off-diagonal blocks contain the state to state coupling elements.

We evaluated the electronic coupling and the transfer rates, for the following processes, labeled according to Scheme 1: 2) electron injection from the dye excited state to the TiO$_2$ slab; 6) the dye excited-state quenching arising from electron injection to the IrO$_2$ catalyst; 3) the hole transfer from the oxidized dye to the IrO$_2$ catalyst; and 5) the electron/hole recombination from TiO$_2$ to the oxidized dye. Processes 2) and 6) were modeled by calculating the electronic coupling between the dye LUMO and the TiO$_2$ and IrO$_2$ manifold of unoccupied states on the dye-TiO$_2$ and dye-IrO$_2$ systems, respectively; process 3) was analyzed in the dye-IrO$_2$ complex, by evaluating the coupling elements between the dye HOMO and the IrO$_2$ manifold of occupied states; and process 5) was investigated by calculating the electronic coupling between the dye HOMO and the TiO$_2$ CB states on the dye-TiO$_2$ system. We note that, with the energy alignment shown in Scheme 1, the only process that were able to model using the complete TiO$_2$/dye/IrO$_2$ assembly, partitioned into IrO$_2$ and dye-TiO$_2$ subsystems, was the hole transfer from the dye HOMO to the IrO$_2$ catalyst.

3. RESULTS AND DISCUSSION

3.1. Modeling the DSPEC Building Blocks: The Isolated TiO$_2$, Dye, and IrO$_2$ Systems. The band offset energetics between the dye and the TiO$_2$/IrO$_2$ oxides play a fundamental role, along with the coupling matrix elements, in determining the rate of (e^-/h^+) transfer reactions, cf. eq 1. Prior to discussing the results for the combined TiO$_2$/dye/IrO$_2$ assemblies, we thus benchmark our computational methodology against available experimental electronic and optical data for the isolated TiO$_2$, dye and IrO$_2$ systems.

The electronic properties of isolated ruthenium dyes in solution are a clear success case of DFT/TDDFT methods employing hybrid functionals.[62,72] Similarly, TiO$_2$ clusters of reasonably large dimensions have been shown to accurately reproduce the structural and electronic features of extended TiO$_2$ surfaces.[62,71,72] The electronic structure and optical properties of IrO$_2$ have been widely investigated both experimentally and theoretically,[87−91] although to the best of our knowledge no IrO$_2$ nanoparticles have been computationally modeled so far. We thus briefly report on the new model proposed here, (IrO$_2$)$_{56}$·2H$_2$O, whose structure is reported in Figure 1. IrO$_2$ crystallizes in the rutile structure, which is retained by our model exposing the majority (110) surfaces, where the degeneracy of the Ir 5d orbitals is lifted by the typical e$_g$/t$_{2g}$ crystal field splitting.[92] A comparison between the experimental XPES spectrum for bulk IrO$_2$ (clean surface) and the calculated valence DOS of our
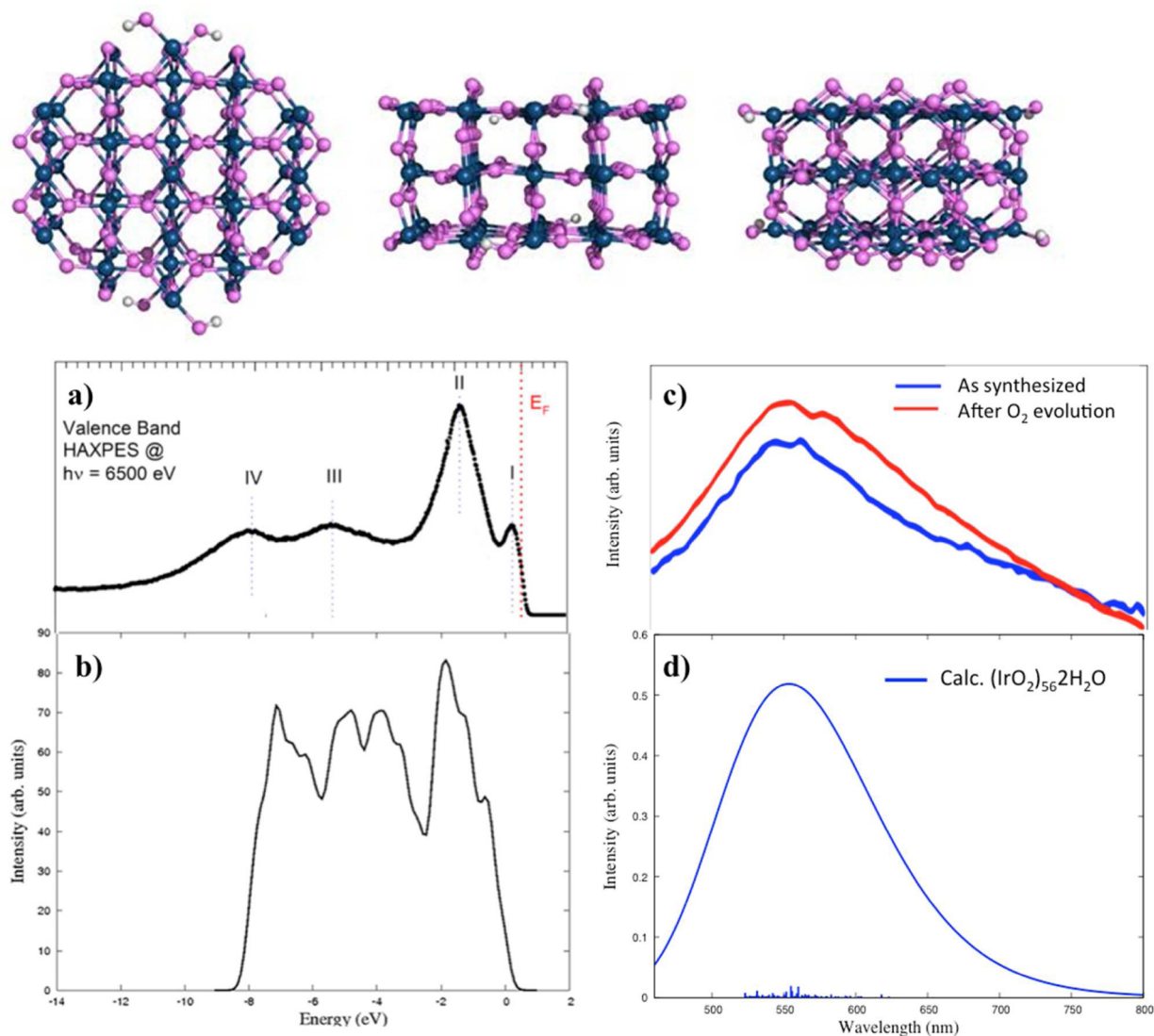
Figure 1. Top: Optimized structure of the $(IrO_2)_{56} \cdot 2H_2O$ nanoparticle model along different views. Dark blue: Ir; magenta: O; white: H atoms. Bottom: (a) Experimental HAXPES spectrum of the IrO_2 valence band adapted from ref 91. (b) Calculated valence DOS of the $(Ir_{56}O_{112} \cdot 2H_2O)$ nanoparticle. (c) Experimental UV−vis absorption spectrum of 2 nm IrO_2 nanoparticles in water solution from ref 95. (d) TDDFT-calculated UV−vis absorption spectrum of the $(Ir_{56}O_{112} \cdot 2H_2O)$ nanoparticle in water. Vertical sticks represent calculated transition wavelengths and oscillator strengths.

model nanoparticle is reported in Figure 1a,b, respectively, showing that the $(IrO_2)_{56} \cdot 2H_2O$ model well reproduces the overall electronic structure of the extended system: the main features of the valence band (labeled as II, III, and IV) are rather precisely predicted as well as the small feature (I) in the correspondence of the Fermi level.[91,93] The $(IrO_2)_{56} \cdot 2H_2O$ HOMO (VB edge) is calculated at −5.58 eV, while the CB edge is found at −5.09 eV. The small energy gap is consistent with the metallic nature of IrO_2, with the band gap opening possibly related to quantum confinement in our model nanoparticle. We thus estimate an oxidation (reduction) potential of 1.14 (0.65) V vs NHE (calculated values obtained against the vacuum are reported to the NHE scale by addition of 4.44), which nicely matches the voltammetry data measured for 2 nm IrO_2 nanoparticles in water solution, ranging from 0.9 ($\approx$pH = 7) to 1.1 V ($\approx$pH = 2).[94] We also calculated by TDDFT several low-lying transitions associated with the visible absorption band of the IrO_2 nanoparticle, mainly corresponding to the $t_{2g} \rightarrow e_g$ transitions of the Ir(IV) cation in the distorted octahedral coordination. We find an absorption maximum at 553 nm, Figure 1d)

in excellent agreement with the experimental absorption at ~550−570 nm, Figure 1c, with a tail down to 800 nm.[95]

A summary of the relevant energy levels for the isolated DSPEC components is reported in Table 1 against known experimental quantities. As it can be noticed, the combination of hybrid DFT/TDDFT values calculated in solution satisfactorily reproduces the experimental energy levels of the dye, TiO_2, and IrO_2, making us confident of the accuracy of the employed methodological setup.

3.2. Modeling the DSPEC Photoanode: The TiO_2-Dye, Dye-IrO_2, and Tethered TiO_2/Dye/IrO_2 Assemblies. The adsorption of ruthenium polypyridyl complexes on the anatase (101) TiO_2 surface by phosphonic acidic groups has been investigated both experimentally[97−102] and theoretically,[103−105] as this anchoring group tends to give stronger binding to metal oxide surfaces, guaranteeing better long-term stability, compared to carboxylic acid groups. The precise binding mode of phosphonic acid to the TiO_2 surface is still to be unequivocally assessed experimentally,[106−108] with theoretical works pointing to either monodentate[104,109] or bidentate bridging modes.[103,110−112]

Table 1. Ground-State Oxidation and Reduction Potential Calculated Using the Koopman's Theorem ($-\varepsilon_{HOMO}$) and ($-\varepsilon_{LUMO}$), Respectively, Along with Excited-State Oxidation Potential Obtained Adding the $S_0 \rightarrow S_1$ Vertical Excitation Energy to ($-\varepsilon_{HOMO}$)[a]

	calc. data		exp. data	
system	HOMO	LUMO/LUMO*	HOMO	LUMO/LUMO*
dye1	−5.96[b]	−2.62/−3.53[b]	−5.74[d]	−3.24[d]
IrO$_2$	−5.58[b]	−5.09/−3.94[b]	−5.34/−5.54[e]	−5.04/−4.64[e]
TiO$_2$	−7.25[b]	−3.28/−3.76[b,c]	−7.04	−3.84[f]

[a]All values are in eV. Experimental data (V vs NHE) are converted in eV against the vacuum by adding 4.44. [b]This work. [c]Ref 71. [d]Ref 34 for [Ru(bpy)$_2$(bpy-PO$_3$H$_2$)$_2$]$^{2+}$. [e]Ref 94. [f]Ref 96.

Here we consider the dye interacting with the TiO$_2$ surface in its partially deprotonated form (2H), ensuring an overall neutral system, with both the phosphonate groups binding via a bidentate anchoring with one hydrogen bond to a surface oxygen atom (Figure 2a), similar to the results of ref 103. The interaction between the phosphonate groups and the anatase surface is rather strong, with O···Ti distances (symmetrical in the two anchoring groups) of 1.98 and 2.12 Å, the latter larger value corresponding to the Ti atom adjacent to the surface oxygen interacting via hydrogen bond with the dye.

On the other side, the dye is tethered to the (IrO$_2$)$_{56}$·2H$_2$O nanoparticle by a bidentate anchoring through a malonic acid group[59] (Figure 2b), with calculated Ir···O distances of 2.20 and 2.23 Å. When considering the TiO$_2$/dye/IrO$_2$ assembly, Figure 2c, the system retains the geometry of the separated TiO$_2$-dye and dye-IrO$_2$ assemblies, leading to an almost orthogonal arrangement of the TiO$_2$ and IrO$_2$ surfaces, Figure 2c. We notice that in principle the malonate group used for IrO$_2$ anchoring could bind TiO$_2$, and similarly the TiO$_2$-binding phosphonate groups may interact with IrO$_2$. While for simplicity we did not consider this "reverse" situation, we believe it might lead to unwanted parasitic excited-state quenching phenomena.

The electronic structure of the TiO$_2$/dye1 interface, Figure 3, presents the typical energy level alignment of Ru(II)-polypyridyl sensitized TiO$_2$.[72,113] The three almost degenerate HOMOs are mainly localized on the dye and are practically identical to those of

the fully protonated isolated molecule, by virtue of the interaction of the anionic phosphonate groups with the TiO$_2$ substrate. A significant broadening of the dye LUMO is calculated, which extends ~0.5 eV above the energy of the TiO$_2$ CB bottom over a range of ~2 eV. This picture is suggestive of strongly coupled electronic states, inducing fast electron injection.

When dye1 is tethered to the IrO$_2$ catalyst, three almost pure dye HOMOs are recognizable at ~0.6–0.7 eV below the IrO$_2$ VB edge, i.e., essentially at the same energy they have in the isolated dye. This energy difference represents the maximum driving force for hole injection into IrO$_2$. The reduced interaction between the dye1 HOMOs and the IrO$_2$ VB, as inferred by the negligible HOMOs broadening in the dye-IrO$_2$ assembly, is an indication of the weak electronic coupling associated with the dye → IrO$_2$ hole transfer process.[15] The dye LUMO broadening upon interaction with the IrO$_2$ CB states, even if considerably weaker than that observed in the TiO$_2$-dye assembly, is still appreciable. These latter data are in line with the measured efficient excited-state quenching observed for IrO$_2$-bound sensitizers.[59]

The calculated UV−vis absorption spectra of the isolated, TiO$_2$- and IrO$_2$-bound dye1, see Figure 4, quantitatively compare with the experimental UV−vis spectra reported by Youngblood et al.[15] The absorption maximum for dye1, associated with the typical metal to ligand charge transfer (MLCT) transition, is predicted at 443 nm, and it is red-shifted to 479 nm when the sensitizer is tethered to the IrO$_2$ catalyst; a slight red-shift is also observed in the experimental spectra, where the maximum for the unbound dye is found at ca. 465 nm, which can be related to the IrO$_2$-induced broadening of the dye LUMO. A small shift at longer wavelengths (459 nm) is also computed for the dye-sensitized TiO$_2$, see Figure 4.

3.3. Interfacial Electron and Hole Transfer Reactions.
Based on the electronic structure picture discussed above, we calculated the rates of the relevant (e^-/h^+) transfer process, namely:

2) Dye* +TiO$_2$ →Dye (h$^+$) + TiO$_2$ (e$^-$)   *(electron injection/semiconductor reduction)*

3) Dye (h$^+$)+ IrO$_2$ → Dye + IrO$_2$ (h$^+$)   *(hole injection/catalyst oxidation)*.

5) TiO$_2$ (e$^-$) + Dye (h$^+$) →TiO$_2$ + Dye   *(electron-hole recombination to the oxidized dye)*

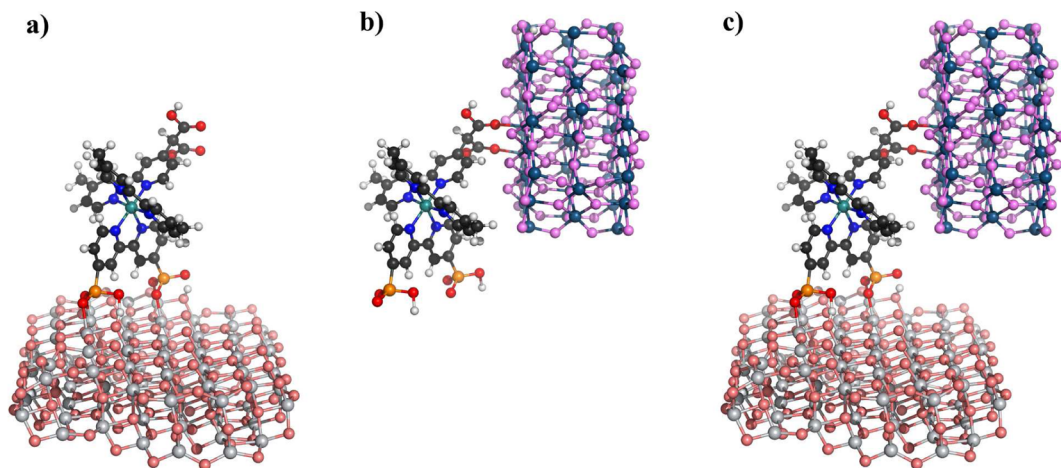6) Dye* +IrO$_2$ →Dye (h$^+$) + IrO$_2$ (e$^-$)   *(oxidative dye excited state quenching to the catalyst)*

Figure 2. Optimized molecular structure of dye1 in its partially deprotonated form (2H), grafted to the (TiO$_2$)$_{82}$ cluster (a), to the (IrO$_2$)$_{56}$·2H$_2$O nanoparticle (b), and tethered across the TiO$_2$ and IrO$_2$ systems, (c). Dark blue: Ir; magenta: O (IrO$_2$); white: H atoms; light gray: Ti; pink: O (TiO$_2$); dark gray: C; red: O (dye); cyan: Ru; blue: N; orange: P.
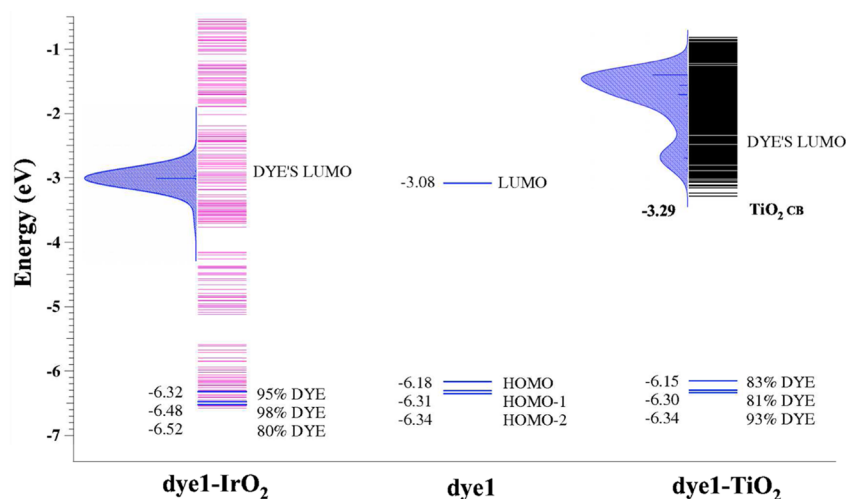
Figure 3. Alignment of energy levels for dye1 at TiO_2/dye and dye/IrO_2 interfaces compared to the energy levels of the stand-alone dye. Dye, IrO_2, and TiO_2 levels are in blue, magenta, and black colors, respectively. The percentages of dye contributions to the HOMOs of TiO_2/dye and dye/IrO_2 assemblies are also reported.
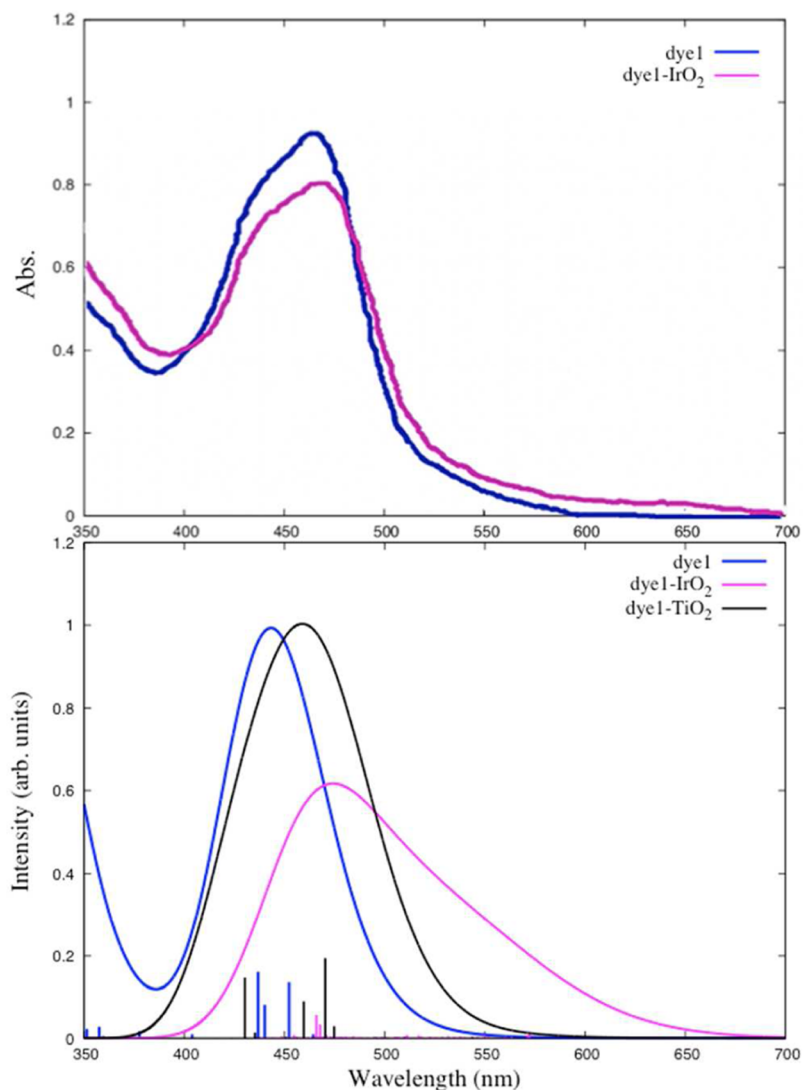

Figure 4. Comparison between the experimental, top, and calculated, bottom, UV−vis absorption spectra of the isolated dye1 in solution and of the TiO_2/dye and dye/IrO_2 interfaces. Experimental data from ref 15.
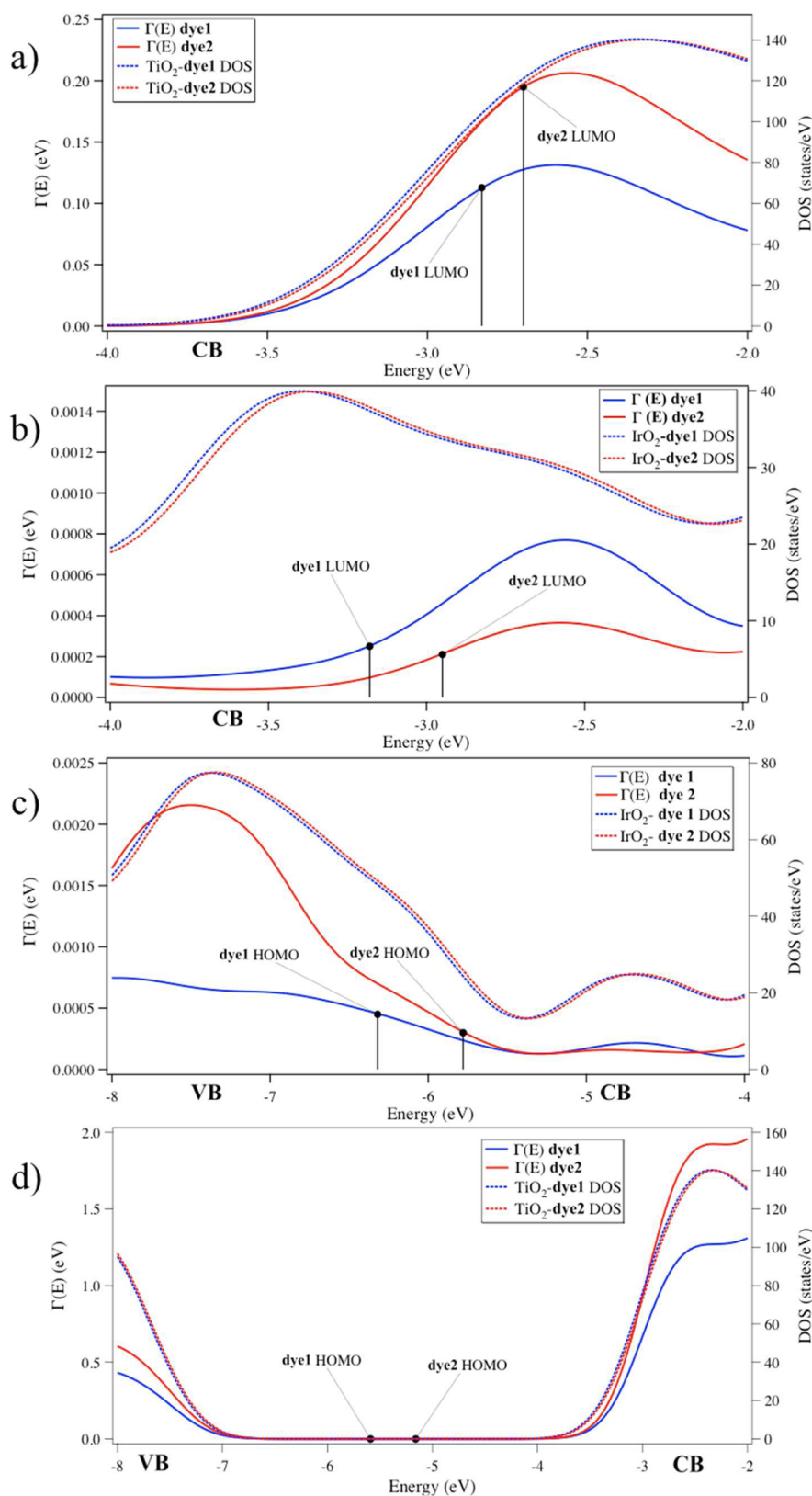
Figure 5. Probability distribution $\Gamma(\varepsilon_k)$ (left scale, solid line, eV) and diabatic DOS (right scale, dashed line, eV^{-1}) for: (a) electron injection from the dye LUMO to the TiO$_2$ CB (process 2); (b) the oxidative dye excited-state quenching to the IrO$_2$ CB (process 6); (c) the hole injection from the dye to the IrO$_2$ VB (process 3); and (d) the electron/hole recombination from the TiO$_2$ CB to the oxidized dye (process 5). The relevant dye energy levels are also reported. Results for dye1 (dye2) are in blue (red) colors.

The results for processes 2, 3, 6, and 5 are reported in Figure 5a−d in terms of probability distribution $\Gamma(\varepsilon_k)$ and

diabatic density of acceptor states, either TiO$_2$ or IrO$_2$, $\rho(\varepsilon_k)$, cf. eq 1, along with the relevant dye energy levels; the $\Gamma(\varepsilon)$ values

extracted at the diabatic dye HOMO/LUMO values, along with the associated calculated injection rates are collected in Table 2, while their comparison with a set of available experimental data is

Table 2. Probability Distributions, $\Gamma(\varepsilon)$ (eV) and DOS (number of states/eV) Calculated at the Diabatic HOMO and LUMO Energies and Associated Injection Rates, k_{inj} (s^{-1})

	Γ (eV)	DOS (states/eV)	k_{inj} (s^{-1})
Dye* + TiO$_2$ → Dye$^+$ + TiO$_2$ (e^-)			
dye1-TiO$_2$	0.1128	106	1.6×10^{14}
dye2-TiO$_2$	0.1940	117	3.3×10^{14}
Dye* + IrO$_2$ → Dye$^+$ + IrO$_2$ (e^-)			
dye1-IrO$_2$	2.5×10^{-4}	37	3.3×10^{11}
dye2-IrO$_2$	1.2×10^{-4}	34	2.0×10^{11}
IrO$_2$ + Dye (h^+) → IrO$_2$ (h^+) + Dye			
dye1-IrO$_2$	4.5×10^{-4}	48	1.0×10^{12}
dye2-IrO$_2$	3.0×10^{-4}	26	5.0×10^{11}
TiO$_2$-dye1-IrO$_2$	2.7×10^{-4}	45	0.5×10^{11}
TiO$_2$-dye2-IrO$_2$	4.6×10^{-4}	37	1.0×10^{12}
TiO$_2$ (e^-) + Dye (h^+) → TiO$_2$ + Dye			
dye1-TiO$_2$	6.3×10^{-11}	1.5×10^{-9}	1.0×10^4
dye2-TiO$_2$	1.2×10^{-11}	5.3×10^{-9}	2.0×10^3

reported in Supporting Information. We notice that in principle these calculations should be performed at the relaxed geometry of the adsorbed dye in either its excited or oxidized state (neglecting relaxation of TiO$_2$/IrO$_2$ upon reduction/oxidation, which is expected to be quite small). For electron injection to TiO$_2$, i.e., process 2, a vertical approximation is usually valid due to the ultrafast (~fs) time scale of this phenomenon. The problem thus mainly involves the hole injection from the oxidized dye to the IrO$_2$ catalyst, process 3, and the excited-state quenching, process 6. To estimate the entity of geometrical relaxation, we have calculated the optimized geometry of the oxidized dye and found only a minimal geometrical relaxation from its ground-state optimized geometry, amounting to only 0.18 eV. The small relaxation energy suggests that a comparably small geometrical relaxation occurs, thus justifying the use of the ground-state geometry.

As it can be noticed from Figure 5 and Table 2, the fastest process (highest k) is the electron injection from the dye LUMO to the TiO$_2$ CB, which is predicted to occur on the fs time scale, in agreement with the experimental <100 fs dynamics observed for this process.[114] For dye1, the hole injection from the dye HOMO to the IrO$_2$ VB is about 3 orders of magnitude less efficient, compare Figure 5a,c and injection rates in Table 2. The rate of the parasitic oxidative dye excited-state quenching to IrO$_2$ is comparable to that of hole injection for dye1, compare Figure 5b,c. Notably, in agreement with the ms experimental time scale (Supporting Information), recombination to the oxidized dye is calculated to be an extremely slow process, Figure 5d, due to the negligible energetic overlap between the dye HOMO and the TiO$_2$ CB (poor DOS of acceptor states).

The quantitative picture extracted from our calculations clearly highlights the problems associated with the functioning of the DSPEC based on dye1, i.e., despite a typically fast electron injection into TiO$_2$, a slow hole injection into IrO$_2$, and a comparable rate of IrO$_2$ reduction by the photoexcited dye are indeed predicted. The reasons underlying this electron/hole transfer picture can be qualitatively understood by looking at the charge density difference occurring upon photoexcitation in dye1, Figure 6c. While the excited electron is delocalized on the

acceptor bipyridines bound to TiO$_2$ through the phosphonate groups, the hole mainly resides on the ruthenium center with a negligible delocalization towards the malonate-functionalized bipyridine through which the dye is anchored to IrO$_2$. This electron/hole localization also explains why the "reverse" anchoring discussed above, with the phosphonate groups binding to IrO$_2$, may be harmful for the DSPEC efficiency, carrying the photoexcited electron closer to the IrO$_2$ thus possibly enhancing the excited-state quenching.

Based on this analysis and inspired by the electronic structure of ruthenium-based solar cells photosensitizers, we sought to introduce a modification into the chemical structure of dye1 which could accomplish at the same time a delocalization of the dye HOMO toward the IrO$_2$-anchoring malonate-functionalized bipyridine and a concomitant shift of the relevant LUMO away from the malonate-functionalized bipyridine, to enhance and suppress, respectively, hole and electron transfer to the IrO$_2$ nanoparticle. To our eyes, the most straightforward way to engineer this sensitizer modification is to introduce a malonate-functionalized cyclometalated phenylpyridine moiety in place of the bipyridine used for IrO$_2$ anchoring, see dye2 structure in Figure 6b. Cyclometalated Ru(II) complexes have been successfully applied as solar cell sensitizers in the dye-sensitized solar cells,[115−119] as they present conveniently tunable HOMOs and LUMO levels and a broad and red-shifted absorption spectrum at same time. Functional to our target, the spatial localization of the HOMO is partly shifted in this class of compounds from the ruthenium center toward the anionic cyclometalated ligand, which is directly connected to the IrO$_2$ catalyst through the malonate ligand. At the same time, the LUMO is shifted away from the IrO$_2$-bound cyclometalated ligand, toward the lower-lying bipyridine unoccupied states. A drawback of introducing such a chemical modification is however the shift at higher energies (i.e., less positive potentials vs NHE) of the dye oxidation potential due to the strong donor character of the anionic phenylpyridine ligand, which can however be tuned to some extent by ligand fluorination.[120]

We have thus computationally assessed the performance of dye2 against the parent dye1 in the (e^-/h^+) transfer processes 2, 3, 6, and 5, see Figure 5a−d and the estimated injection rates in Table 2. Notably, the proposed chemical design improves both the probability function for electron and hole transfer rates to TiO$_2$ and IrO$_2$, Figure 5a−c, respectively, leading at the same time to its reduction for the dye excited-state quenching to IrO$_2$, Figure 5b. We also notice that hole injection into the IrO$_2$ catalyst could be made significantly more efficient if one were able to further down-shift the dye2 HOMOs, thus sampling a region of higher IrO$_2$ VB DOS, Figure 5c. In other words, the loss due to the negative (vs NHE) HOMO shift of dye2 compared to dye1 is partly compensated by the strong increase in the electronic coupling with the IrO$_2$ VB due to the ligand engineering, since the IrO$_2$ DOS is essentially unaltered by attachment of different dyes.

An overall picture of the energy levels of the complete TiO$_2$/dye/IrO$_2$ DSPEC photoanode for dye1 and dye2 is reported in Figure 6e,f. Notably, our computational approach quantitatively describes the expected energetics of the investigated DSPEC architecture, showing the dye HOMOs within the IrO$_2$ VB as well as the dye LUMOs distributed above the TiO$_2$ CB. As it can be noticed, the dye2 HOMOs show a considerably broader distribution than those of dye1, reflecting their stronger interaction with the IrO$_2$ VB, despite sampling a relatively lower IrO$_2$ VB DOS.
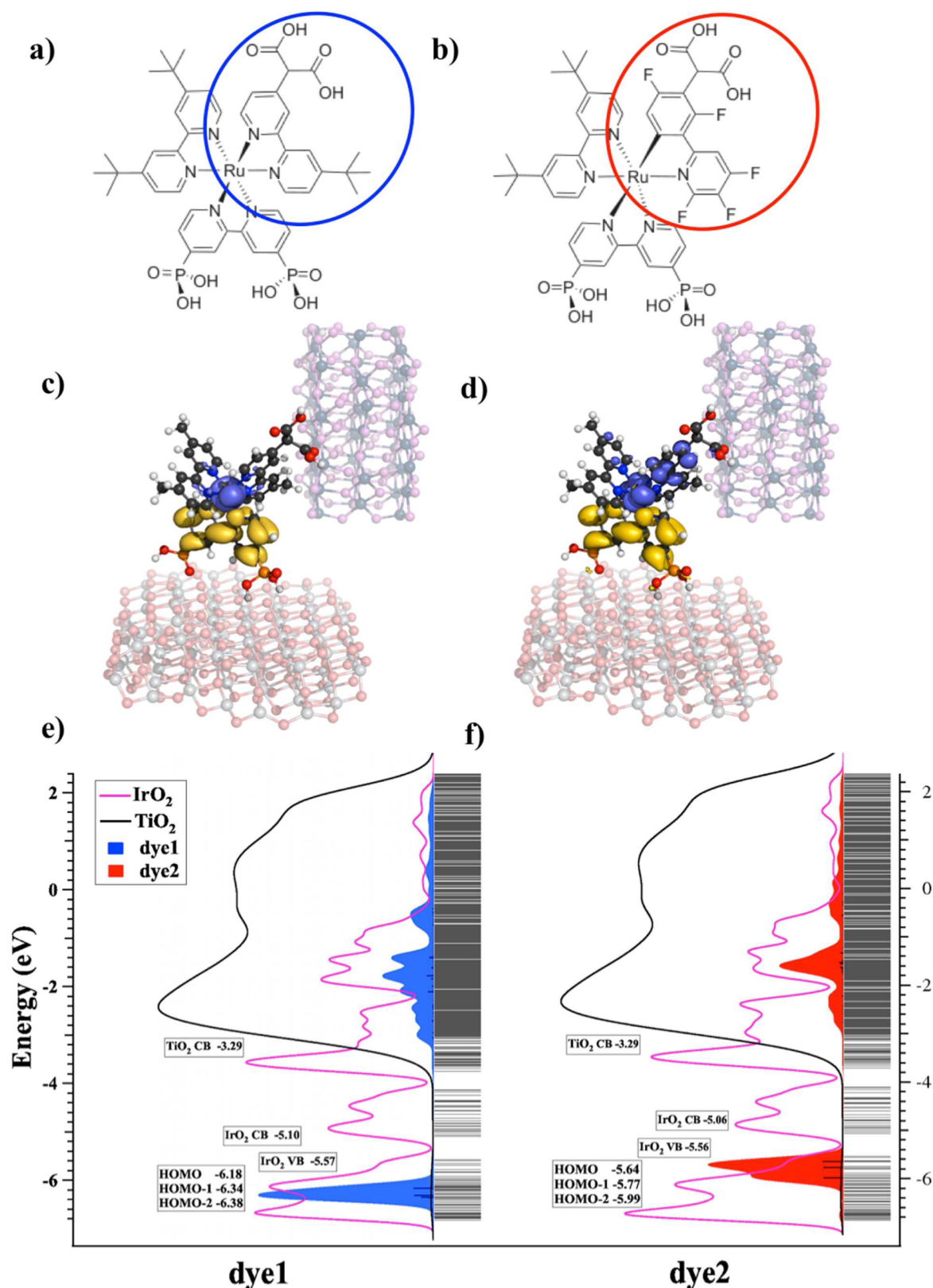
Figure 6. Molecular structure of dye1 (a) and of the cyclometalated Ru(II) dye2 (b) and their HOMO−LUMO density difference isosurfaces (blue and yellow lobes indicate density depletion and accumulation respectively) (c and d). (e and f) Alignment of energy levels in the TiO₂/dye/IrO₂ assemblies based on dye1 and dye2, respectively.

4. SUMMARY AND CONCLUSIONS

In summary, we have investigated for the first time, by state of the art computational modeling the crucial triple TiO₂/dye/IrO₂

heterointerface characterizing a typical DSPEC photoanode architecture for water splitting. We have considered a prototypical DSPEC,[15] consisting of a bifunctional heteroleptic

Ru(II) sensitizer, showing phosphonate groups for TiO_2 anchoring and a malonate group to bind to hydrated iridium dioxide ($IrO_2 \cdot nH_2O$) nanoparticles. Our quantitative analysis of the critical electron/hole transfer rates based on extended models of the prototypical system has unveiled the crucial electronic features underlying the device functioning, highlighting the slow hole injection to IrO_2 and the fast parasitic dye excited-state quenching to IrO_2 as the major sources of the low device efficiency, fully in line with the experimental evidence.[15,59] Based on this information, we have designed and computationally probed a new cyclometalated dye which showed globally improved interfacial properties compared to the parent dye, highlighting the possible design routes toward new and more efficient materials for water splitting.

■ ASSOCIATED CONTENT

ⓢ Supporting Information

Comparison between calculated and experimental rates. Optimized geometrical structures. This material is available free of charge via the Internet at http://pubs.acs.org.

■ AUTHOR INFORMATION

Corresponding Authors
*chiara@thch.unipg.it
*filippo@thch.unipg.it

Notes
The authors declare no competing financial interest.

■ ACKNOWLEDGMENTS

■ REFERENCES

(1) Grätzel, M. *Acc. Chem. Res.* **2009**, *42*, 1788−1798.
(2) Young, K. J.; Martini, L. A.; Milot, R. L.; Snoeberger Iii, R. C.; Batista, V. S.; Schmuttenmaer, C. A.; Crabtree, R. H.; Brudvig, G. W. *Coord. Chem. Rev.* **2012**, *256*, 2503−2520.
(3) Hamann, T. W. *Nat. Mater.* **2014**, *13*, 3−4.
(4) Concepcion, J. J.; House, R. L.; Papanikolas, J. M.; Meyer, T. J. *Proc. Natl. Acad. Sci. U.S.A.* **2012**, *109*, 15560−15564.
(5) Fujishima, A.; Honda, K. *Nature* **1972**, *238*, 37−38.
(6) Kato, H.; Asakura, K.; Kudo, A. *J. Am. Chem. Soc.* **2003**, *125*, 3082−3089.
(7) Chen, X.; Shen, S.; Guo, L.; Mao, S. S. *Chem. Rev.* **2010**, *110*, 6503−6570.
(8) Higashi, M.; Domen, K.; Abe, R. *En. Environ. Sci.* **2011**, *4*, 4138−4147.
(9) Chen, Z.; Jaramillo, T. F.; Deutsch, T. G.; Kleiman-Shwarsctein, A.; Forman, A. J.; Gaillard, N.; Garland, R.; Takanabe, K.; Heske, C.; Sunkara, M.; McFarland, E. W.; Domen, K.; Miller, E. L.; Turner, J. A.; Dinh, H. N. *J. Mater. Res.* **2010**, *25*, 3−16.
(10) Minggu, L. J.; Wan Daud, W. R.; Kassim, M. B. *Int. J. Hydrogen Energy* **2010**, *35*, 5233−5244.
(11) Cristino, V.; Caramori, S.; Argazzi, R.; Meda, L.; Marra, G. L.; Bignozzi, C. A. *Langmuir* **2011**, *27*, 7276−7284.
(12) Yang, J.; Wang, D.; Han, H.; Li, C. *Acc. Chem. Res.* **2013**, *46*, 1900−1909.
(13) Higashi, M.; Domen, K.; Abe, R. *J. Am. Chem. Soc.* **2012**, *134*, 6968−6971.
(14) Reece, S. Y.; Hamel, J. A.; Sung, K.; Jarvi, T. D.; Esswein, A. J.; Pijpers, J. J. H.; Nocera, D. G. *Science* **2011**, *334*, 645−648.
(15) Youngblood, W. J.; Lee, S.-H. A.; Kobayashi, Y.; Hernandez-Pagan, E. A.; Hoertz, P. G.; Moore, T. A.; Moore, A. L.; Gust, D.; Mallouk, T. E. *J. Am. Chem. Soc.* **2009**, *131*, 926−927.
(16) Youngblood, W. J.; Lee, S.-H. A.; Maeda, K.; Mallouk, T. E. *Acc. Chem. Res.* **2009**, *42*, 1966−1973.
(17) Swierk, J. R.; Mallouk, T. E. *Chem. Soc. Rev.* **2013**, *42*, 2357−2387.
(18) Gao, Y.; Zhang, L.; Ding, X.; Sun, L. *Phys. Chem. Chem. Phys.* **2014**, *16*, 12008−12013.
(19) Moore, G. F.; Blakemore, J. D.; Milot, R. L.; Hull, J. F.; Song, H.-e.; Cai, L.; Schmuttenmaer, C. A.; Crabtree, R. H.; Brudvig, G. W. *Energy Environ. Sci.* **2011**, *4*, 2389−2392.
(20) Li, L.; Duan, L.; Xu, Y.; Gorlov, M.; Hagfeldt, A.; Sun, L. *Chem. Commun.* **2010**, *46*, 7307−7309.
(21) Zhao, Y.; Swierk, J. R.; Megiatto, J. D.; Sherman, B.; Youngblood, W. J.; Qin, D.; Lentz, D. M.; Moore, A. L.; Moore, T. A.; Gust, D.; Mallouk, T. E. *Proc. Natl. Acad. Sci. U.S.A.* **2012**, *109*, 15612−15616.
(22) Hanson, K.; Torelli, D. A.; Vannucci, A. K.; Brennaman, M. K.; Luo, H.; Alibabaei, L.; Song, W.; Ashford, D. L.; Norris, M. R.; Glasson, C. R. K.; Concepcion, J. J.; Meyer, T. J. *Angew. Chem., Int. Ed.* **2012**, *51*, 12782−12785.
(23) Alibabaei, L.; Brennaman, M. K.; Norris, M. R.; Kalanyan, B.; Song, W.; Losego, M. D.; Concepcion, J. J.; Binstead, R. A.; Parsons, G. N.; Meyer, T. J. *Proc. Natl. Acad. Sci. U.S.A.* **2013**, *110*, 20008−20013.
(24) Yu, Z.; Li, F.; Sun, L. *Energy Environ. Sci.* **2015**, *8*, 760−775.
(25) Wu, L.-Z.; Chen, B.; Li, Z.-J.; Tung, C.-H. *Acc. Chem. Res.* **2014**, *47*, 2177−2185.
(26) Li, G.; Sproviero, E. M.; Snoeberger Iii, R. C.; Iguchi, N.; Blakemore, J. D.; Crabtree, R. H.; Brudvig, G. W.; Batista, V. S. *Energy Environ. Sci.* **2009**, *2*, 230−238.
(27) Wasylenko, D. J.; Palmer, R. D.; Berlinguette, C. P. *Chem. Commun.* **2013**, *49*, 218−227.
(28) Klepser, B. M.; Bartlett, B. M. *J. Am. Chem. Soc.* **2014**, *136*, 1694−1697.
(29) Berardi, S.; Drouet, S.; Francas, L.; Gimbert-Surinach, C.; Guttentag, M.; Richmond, C.; Stoll, T.; Llobet, A. *Chem. Soc. Rev.* **2014**, *43*, 7501−7519.
(30) Wiechen, M.; Spiccia, L. *Chem. Catal. Chem.* **2014**, *6*, 439−441.
(31) Yin, Q.; Tan, J. M.; Besson, C.; Geletii, Y. V.; Musaev, D. G.; Kuznetsov, A. E.; Luo, Z.; Hardcastle, K. I.; Hill, C. L. *Science* **2010**, *328*, 342−345.
(32) Duan, L.; Araujo, C. M.; Ahlquist, M. S. G.; Sun, L. *Proc. Natl. Acad. Sci. U.S.A.* **2010**, *109*, 15584−15588.
(33) Norris, M. R.; Concepcion, J. J.; Fang, Z.; Templeton, J. L.; Meyer, T. J. *Angew. Chem.* **2013**, *125*, 13825−13828.
(34) Gao, Y.; Ding, X.; Liu, J.; Wang, L.; Lu, Z.; Li, L.; Sun, L. *J. Am. Chem. Soc.* **2013**, *135*, 4219−4222.
(35) Duan, L.; Bozoglian, F.; Mandal, S.; Stewart, B.; Privalov, T.; Llobet, A.; Sun, L. *Nat. Chem.* **2012**, *4*, 418−423.
(36) Lv, H.; Geletii, Y. V.; Zhao, C.; Vickers, J. W.; Zhu, G.; Luo, Z.; Song, J.; Lian, T.; Musaev, D. G.; Hill, C. L. *Chem. Soc. Rev.* **2012**, *41*, 7572−7589.
(37) Kärkäs, M. D.; Verho, O.; Johnston, E. V.; Åkermark, B. *Chem. Rev.* **2014**, *114*, 11863−12001.
(38) Kiwi, J.; Grätzel, M. *Angew. Chem., Int. Ed.* **1979**, *18*, 624−626.
(39) Hara, M.; Waraksa, C. C.; Lean, J. T.; Lewis, B. A.; Mallouk, T. E. *J. Phys. Chem. A* **2000**, *104*, 5275−5280.
(40) Blakemore, J. D.; Gray, H. B.; Winkler, J. R.; Müller, A. M. *ACS Catal.* **2013**, *3*, 2497−2500.
(41) Jiao, F.; Frei, H. *Angew. Chem., Int. Ed.* **2009**, *48*, 1841−1844.
(42) Osterloh, F. E. *Chem. Soc. Rev.* **2013**, *42*, 2294−2320.
(43) Harriman, A.; Pickering, I. J.; Thomas, J. M.; Christensen, P. A. *J. Chem. Soc, Faraday Trans 1* **1988**, *84*, 2795−2806.
(44) Lattach, Y.; Rivera, J. F.; Bamine, T.; Deronzier, A.; Moutet, J.-C. *ACS Appl. Mater. Interfaces* **2014**, *6*, 12852−12859.
(45) Bledowski, M.; Wang, L.; Neubert, S.; Mitoraj, D.; Beranek, R. *J. Phys. Chem. C* **2014**, *118*, 18951−18961.
(46) Swierk, J. R.; McCool, N. S.; Saunders, T. P.; Barber, G. D.; Strayer, M. E.; Vargas-Barbosa, N. M.; Mallouk, T. E. *J. Phys. Chem. C* **2014**, *118*, 17046−17053.
(47) Zhao, Y.; Hernandez-Pagan, E. A.; Vargas-Barbosa, N. M.; Dysart, J. L.; Mallouk, T. E. *J. Phys. Chem. Lett.* **2011**, *2*, 402−406.

(48) Swierk, J. R.; McCool, N. S.; Saunders, T. P.; Barber, G. D.; Mallouk, T. E. *J. Am. Chem. Soc.* **2014**, *136*, 10974−10982.

(49) Suntivich, J.; May, K. J.; Gasteiger, H. A.; Goodenough, J. B.; Shao-Horn, Y. *Science* **2011**, *334*, 1383−1385.

(50) Meyer, G. J. *Inorg. Chem.* **2005**, *44*, 6852−6864.

(51) Griffith, M. J.; Sunahara, K.; Wagner, P.; Wagner, K.; Wallace, G. G.; Officer, D. L.; Furube, A.; Katoh, R.; Mori, S.; Mozer, A. J. *Chem. Commun.* **2012**, *48*, 4145−4162.

(52) Martini, L. A.; Moore, G. F.; Milot, R. L.; Cai, L. Z.; Sheehan, S. W.; Schmuttenmaer, C. A.; Brudvig, G. W.; Crabtree, R. H. *J. Phys. Chem. C* **2013**, *117*, 14526−14533.

(53) Swierk, J. R.; Méndez-Hernández, D. D.; McCool, N. S.; Liddell, P.; Terazono, Y.; Pahk, I.; Tomlin, J. J.; Oster, N. V.; Moore, T. A.; Moore, A. L.; Gust, D.; Mallouk, T. E. *Proc. Natl. Acad. Sci. U.S.A.* **2015**, *109*, 15612−15616.

(54) Xiao, F.-X.; Miao, J.; Wang, H.-Y.; Yang, H.; Chen, J.; Liu, B. *Nanoscale* **2014**, *6*, 6727−6737.

(55) Alibabaei, L.; Luo, H.; House, R. L.; Hoertz, P. G.; Lopez, R.; Meyer, T. J. *J. Mater. Chem. A* **2013**, *1*, 4133−4145.

(56) Brimblecombe, R.; Koo, A.; Dismukes, G. C.; Swiegers, G. F.; Spiccia, L. *J. Am. Chem. Soc.* **2010**, *132*, 2892−2894.

(57) Xiang, X.; Fielden, J.; Rodríguez-Córdoba, W.; Huang, Z.; Zhang, N.; Luo, Z.; Musaev, D. G.; Lian, T.; Hill, C. L. *J. Phys. Chem. C* **2013**, *117*, 918−926.

(58) Fan, K.; Li, F.; Wang, L.; Daniel, Q.; Gabrielsson, E.; Sun, L. *Phys. Chem. Chem. Phys.* **2014**, *16*, 25234−25240.

(59) Hoertz, P. G.; Kim, Y.-I.; Youngblood, W. J.; Mallouk, T. E. *J. Phys. Chem. B* **2007**, *111*, 6845−6856.

(60) Lopez, A. M.; Natali, M.; Pizzolato, E.; Chiorboli, C.; Bonchio, M.; Sartorel, A.; Scandola, F. *Phys. . Chem. Chem. Phys.* **2014**, *16*, 12000−12007.

(61) Pastore, M.; De Angelis, F. Modeling Materials and Processes in Dye-Sensitized Solar Cells: Understanding the Mechanism. *Improving the Efficiency*; Springer: Berlin Heidelberg, 2013; pp 1−86.

(62) De Angelis, F. *Acc. Chem. Res.* **2014**, *47*, 3349−3360.

(63) Sproviero, E. M.; Gascón, J. A.; McEvoy, J. P.; Brudvig, G. W.; Batista, V. S. *J. Am. Chem. Soc.* **2008**, *130*, 3428−3442.

(64) Yang, X.; Hall, M. B. *J. Am. Chem. Soc.* **2009**, *132*, 120−130.

(65) Mavros, M. G.; Tsuchimochi, T.; Kowalczyk, T.; McIsaac, A.; Wang, L.-P.; Voorhis, T. V. *Inorg. Chem.* **2014**, *53*, 6386−6397.

(66) Sobolewski, A. L.; Domcke, W. *J. Phys. Chem. A* **2008**, *112*, 7311−7313.

(67) Rivalta, I.; Brudvig, G. W.; Batista, V. S. Computational Studies of the Oxygen-Evolving Complex of Photosystem II and Biomimetic Oxomanganese Complexes for Renewable Energy Applications. In *Applications of Molecular Modeling to Challenges in Clean Energy*; American Chemical Society: Washington, DC, 2013; Vol. *1133*, pp 203−215.

(68) Sproviero, E. M.; Shinopoulos, K.; Gasc√≥n, J. A.; McEvoy, J. P.; Brudvig, G. W.; Batista, V. S. *Philosophical Transactions of the Royal Society B: Biological Sciences* **2008**, *363*, 1149−1156.

(69) Vittadini, A.; Selloni, A.; Rotzinger, F. P.; Grätzel, M. *Phys. Rev. Lett.* **1998**, *81*, 2954−2957.

(70) Lundqvist, M. J.; Nilsing, M.; Persson, P.; Lunel, S. *Int. J. Quantum Chem.* **2006**, *106*, 3214−3234.

(71) De Angelis, F.; Fantacci, S.; Mosconi, E.; Nazeeruddin, M. K.; Grätzel, M. *J. . Phys. Chem. C* **2011**, *115*, 8825−8831.

(72) Pastore, M.; Selloni, A.; Fantacci, S.; Angelis, F. Electronic and Optical Properties of Dye-Sensitized TiO$_2$ Interfaces. In *Topics in Current Chemistry*; Springer: Berlin Heidelberg, 2014; pp 1−45.

(73) te Velde, G.; Bickelhaupt, F. M.; Baerends, E. J.; Fonseca Guerra, C.; van Gisbergen, S. J. A.; Snijders, J. G.; Ziegler, T. *J. Comput. Chem.* **2001**, *22*, 931−967.

(74) Becke, A. D. *Phys. Rev. A* **1988**, *38*, 3098−3100.

(75) Perdew, J. P. *Phys. Rev. B* **1986**, *33*, 8822−8824.

(76) Cossi, M.; Rega, N.; Scalmani, G.; Barone, V. *J. Comput. Chem.* **2003**, *24*, 669−681.

(77) Barone, V.; Cossi, M. *J. Phys. Chem. A* **1998**, *102*, 1995−2001.

(78) Frisch, M. J.; Trucks, G. W.; Schlegel, H. B.; Scuseria, G. E.; Robb, M. A.; Cheeseman, J. R.; Scalmani, G.; Barone, V.; Mennucci, B.; Petersson, G. A.; Nakatsuji, H.; Caricato, M.; Li, X.; Hratchian, H. P.; Izmaylov, A. F.; Bloino, J.; Zheng, G.; Sonnenberg, J. L.; Hada, M.; Ehara, M.; Toyota, K.; Fukuda, R.; Hasegawa, J.; Ishida, M.; Nakajima, T.; Honda, Y.; Kitao, O.; Nakai, H.; Vreven, T.; Montgomery, J. A., Jr.; Peralta, J. E.; Ogliaro, F.; Bearpark, M.; Heyd, J. J.; Brothers, E.; Kudin, K. N.; Staroverov, V. N.; Kobayashi, R.; Normand, J.; Raghavachari, K.; Rendell, A.; Burant, J. C.; Iyengar, S. S.; Tomasi, J.; Cossi, M.; Rega, N.; Millam, N. J.; Klene, M.; Knox, J. E.; Cross, J. B.; Bakken, V.; Adamo, C.; Jaramillo, J.; Gomperts, R.; Stratmann, R. E.; Yazyev, O.; Austin, A. J.; Cammi, R.; Pomelli, C.; Ochterski, J. W.; Martin, R. L.; Morokuma, K.; Zakrzewski, V. G.; Voth, G. A.; Salvador, P.; Dannenberg, J.J.; Dapprich, S.; Daniels, A. D.; Farkas, Ö.; Foresman, J. B.; Ortiz, J. V.; Cioslowski, J.; Fox, D. J. *Gaussian 09*, revision D.1; Gaussian, Inc.: Wallingford, CT, 2009.

(79) Dunning, T. H. J.; Hay, P. J. *Modern Theoretical Chemistry*; Plenum: New York; 1977; Vol. 3.

(80) Hay, P. J.; Wadt, W. R. *J. Chem. Phys.* **1985**, *82*, 299−310.

(81) Wadt, W. R.; Hay, P. J. *J. Chem. Phys.* **1985**, *82*, 284−298.

(82) Hay, P. J.; Wadt, W. R. *J. Chem. Phys.* **1985**, *82*, 270−283.

(83) Kondov, I.; Čížek, M.; Benesch, C.; Wang, H.; Thoss, M. *J. Phys. Chem. C* **2007**, *111*, 11970−11981.

(84) Li, J.; Wang, H.; Persson, P.; Thoss, M. *J. Chem. Phys.* **2012**, *137*, 22A529−516.

(85) Agrawal, S.; Leijtens, T.; Ronca, E.; Pastore, M.; Snaith, H.; De Angelis, F. *J. Mater. Chem. A* **2013**, *1*, 14675−14685.

(86) Ronca, E.; Marotta, G.; Pastore, M.; De Angelis, F. *J. Phys. Chem. C* **2014**, *118*, 16927−16940.

(87) de Almeida, J. S.; Ahuja, R. *Phys. Rev. B* **2006**, *73*, 165102.

(88) Miao, M. S.; Seshadri, R. *J. Phys.: Condens. Matter* **2012**, *24*, 215503.

(89) Clancy, J. P.; Chen, N.; Kim, C. Y.; Chen, W. F.; Plumb, K. W.; Jeon, B. C.; Noh, T. W.; Kim, Y.-J. *Phys. Rev. B* **2012**, *86*, 195131.

(90) Hirata, Y.; Ohgushi, K.; Yamaura, J.-i.; Ohsumi, H.; Takeshita, S.; Takata, M.; Arima, T.-h. *Phys. Rev. B* **2013**, *87*, 161111.

(91) Kahk, J. M.; Poll, C. G.; Oropeza, F. E.; Ablett, J. M.; Céolin, D.; Rueff, J.-P.; Agrestini, S.; Utsumi, Y.; Tsuei, K. D.; Liao, Y. F.; Borgatti, F.; Panaccione, G.; Regoutz, A.; Egdell, R. G.; Morgan, B. J.; Scanlon, D. O.; Payne, D. J. *Phys. Rev. Lett.* **2014**, *112*, 117601.

(92) Goodenough, J. B. *J. Solid. State Chem.* **1971**, *3*, 490−500.

(93) Riga, J.; Tenret-Noël, C.; Pireaux, J. J.; Caudano, R.; Verbist, J. J.; Gobillon, Y. *Phys. Scri.* **1977**, *16*, 351.

(94) Gambardella, A. A.; Bjorge, N. S.; Alspaugh, V. K.; Murray, R. W. *J. Phys. Chem. C* **2011**, *115*, 21659−21665.

(95) Frame, F. A.; Townsend, T. K.; Chamousis, R. L.; Sabio, E. M.; Dittrich, T.; Browning, N. D.; Osterloh, F. E. *J. Am. Chem. Soc.* **2011**, *133*, 7264−7267.

(96) Kavan, L.; Grätzel, M.; Gilbert, S. E.; Klemenz, C.; Scheel, H. J. *J. Am. Chem. Soc.* **1996**, *118*, 6716−6723.

(97) Pechy, P.; Rotzinger, F. P.; Nazeeruddin, M. K.; Kohle, O.; Zakeeruddin, S. M.; Humphry-Baker, R.; Gratzel, M. *J. Chem. Soc. Chem. Comm.* **1995**, 65−66.

(98) Zakeeruddin, S. M.; Nazeeruddin, M. K.; Pechy, P.; Rotzinger, F. P.; Humphry-Baker, R.; Kalyanasundaram, K.; Grätzel, M.; Shklover, V.; Haibach, T. *Inorg. Chem.* **1997**, *36*, 5937−5946.

(99) Zabri, H.; Gillaizeau, I.; Bignozzi, C. A.; Caramori, S.; Charlot, M.-F.; Cano-Boquera, J.; Odobel, F. *Inorg. Chem.* **2003**, *42*, 6655−6666.

(100) Gillaizeau-Gauthier, I.; Odobel, F.; Alebbi, M.; Argazzi, R.; Costa, E.; Bignozzi, C. A.; Qu, P.; Meyer, G. J. *Inorg. Chem.* **2001**, *40*, 6073−6079.

(101) Bae, E.; Choi, W.; Park, J.; Shin, H. S.; Kim, S. B.; Lee, J. S. *J. Phys. Chem. B* **2004**, *108*, 14093−14101.

(102) Hanson, K.; Brennaman, M. K.; Luo, H.; Glasson, C. R. K.; Concepcion, J. J.; Song, W.; Meyer, T. J. *ACS Appl. Mater. Interfaces* **2012**, *4*, 1462−1469.

(103) Luschtinetz, R.; Frenzel, J.; Milek, T.; Seifert, G. *J. Phys. Chem. C* **2009**, *113*, 5730−5740.

(104) Nilsing, M.; Lunell, S.; Persson, P.; Ojamäe, L. *Surf. Sci.* **2005**, *582*, 49−60.

(105) Lundqvist, M. J.; Nilsing, M.; Lunell, S.; Åkermark, B.; Persson, P. *J. Phys. Chem. B* **2006**, *110*, 20513−20525.

(106) Guerrero, G.; Mutin, P. H.; Vioux, A. *Chem. Mater.* **2001**, *13*, 4367−4373.

(107) Pawsey, S.; Yach, K.; Reven, L. *Langmuir* **2002**, *18*, 5205−5212.

(108) Lafont, U.; Simonin, L.; Gaberscek, M.; Kelder, E. M. *J. Pow. Sourc.* **2007**, *174*, 1104−1108.

(109) Nilsing, M.; Persson, P.; Lunell, S.; Ojamäe, L. *J. Phys. Chem. C* **2007**, *111*, 12116−12123.

(110) Nilsing, M.; Persson, P.; Ojamäe, L. *Chem. Phys. Lett.* **2005**, *415*, 375−380.

(111) Pang, C. L.; Watkins, M.; Cabailh, G.; Ferrero, S.; Ngo, L. T.; Chen, Q.; Humphrey, D. S.; Shluger, A. L.; Thornton, G. *J. Phys. Chem. C* **2010**, *114*, 16983−16988.

(112) Coppens, P.; Chen, Y.; Trzop, E. *Chem. Rev.* **2014**, *114*, 9645−9661.

(113) De Angelis, F.; Fantacci, S.; Selloni, A. *Nanotechnology* **2008**, *19*, 424002.

(114) She, C.; Guo, J.; Irle, S.; Morokuma, K.; Mohler, D. L.; Zabri, H.; Odobel, F.; Youm, K.-T.; Liu, F.; Hupp, J. T.; Lian, T. *J. Phys. Chem. A* **2007**, *111*, 6832−6842.

(115) Bessho, T.; Yoneda, E.; Yum, J.-H.; Guglielmi, M.; Tavernelli, I.; Imai, H.; Rothlisberger, U.; Nazeeruddin, M. K.; Grätzel, M. *J. Am. Chem. Soc.* **2009**, *131*, 5930−5934.

(116) Bomben, P. G.; Koivisto, B. D.; Berlinguette, C. P. *Inorg. Chem.* **2010**, *49*, 4960−4971.

(117) Colombo, A.; Dragonetti, C.; Valore, A.; Coluccini, C.; Manfredi, N.; Abbotto, A. *Polyhedron* **2014**, *82*, 50−56.

(118) Schulze, B.; Brown, D. G.; Robson, K. C. D.; Friebe, C.; Jäger, M.; Birckner, E.; Berlinguette, C. P.; Schubert, U. S. *Chem.—Eur. J.* **2013**, *19*, 14171−14180.

(119) Chitumalla, R. K.; Gupta, K. S. V.; Malapaka, C.; Fallahpour, R.; Islam, A.; Han, L.; Kotamarthi, B.; Singh, S. P. *Phys. Chem. Chem. Phys.* **2014**, *16*, 2630−2640.

(120) De Angelis, F.; Fantacci, S.; Evans, N.; Klein, C.; Zakeeruddin, S. M.; Moser, J.-E.; Kalyanasundaram, K.; Bolink, H. J.; Grätzel, M.; Nazeeruddin, M. K. *Inorg. Chem.* **2007**, *46*, 5989−6001.